Polymer 52 (2011) 529–539

Contents lists available at ScienceDirect

Polymer

journal homepage: www.elsevier.com/locate/polymer

# Biaxial elastic–viscoplastic behavior of Nafion membranes

Meredith N. Silberstein, Priam V. Pillai, Mary C. Boyce*

*MIT Department of Mechanical Engineering, 77 Massachusetts Avenue, Cambridge, MA 02139, USA*

ARTICLE INFO

*Article history:*
Received 28 September 2010
Received in revised form
16 November 2010
Accepted 20 November 2010
Available online 3 December 2010

*Keywords:*
Polymer mechanics
Nafion
Biaxial

ABSTRACT

Durability is a major limitation of current proton exchange membrane fuel cells. Mechanical stress due to hygro-thermal cycling is one failure mechanism of the polymer electrolyte membrane (PEM). In a fuel cell the PEM is highly constrained in the membrane plane and relatively unconstrained in the through-thickness direction, leading to primarily biaxial loading upon hygro-thermal cycling. The rate, temperature, and hydration dependent elastic–viscoplastic mechanical behavior of Nafion, the benchmark PEM, has been extensively investigated in uniaxial tension in prior work which also served as a data basis for a three dimensional constitutive model. Here, the important effects of the biaxiality of the loading conditions on the elastic–viscoplastic Nafion stress–strain behavior are investigated for the first time via experiments and simulation. Biaxial stress–strain behaviors were shown to exhibit similar features to uniaxial behavior including linear elasticity followed by a highly non-linear transition to yield followed by post-yield strain hardening with highly non-linear unloading and reloading; these features were each quantitatively dependent on the biaxiality of the loading conditions. The constitutive model was found to successfully quantitatively predict the loading behavior and its dependence on biaxiality. The constitutive model was also found to predict the magnitude of the yield shoulder during unloading and reloading, but to underestimate the gradual nature of both the forward and reverse plastic deformation processes as well as the strain recovery at zero load. These errors are consistent with those seen in the uniaxial model indicating that the framework used to incorporate the uniaxial behavior into a three dimensional model is capable of predicting the biaxial deformation response of the membrane.

© 2010 Elsevier Ltd. All rights reserved.

## 1. Background

The proton exchange membrane fuel cell (PEMFC) is a promising clean technology for converting chemical energy into electrical energy, particularly for transportation. Insufficient durability is one of the major factors inhibiting the widespread distribution of this technology. In particular, the membrane electrode assembly (MEA), which consists of a selectively permeable polymer electrolyte membrane (PEM) with a catalyst layer and porous carbon electrode support on each side, is known to fail under the cyclic operating conditions of automobiles. The PEM is responsible for conducting protons while preventing hydrogen and oxygen gas crossover. Until recently, durability research has focused on preventing degradation due to chemical attacks, however, with progress against chemical attacks focus has shifted to the increasingly significant mechanical degradation modes [1]. Cyclic mechanical loading results from water content driven swelling and deswelling of the membrane within the partially constrained environment of the fuel cell. Since the membrane in a fuel cell is highly constrained in the membrane plane and relatively unconstrained in the through-thickness direction, this cyclic loading will be primarily biaxial in nature. Biaxial loading also has relevance for polymeric membranes more generally given their increasing use in separation and transport applications.

In our prior work [2], the uniaxial tensile behavior of Nafion was characterized under both monotonic and cyclic loading as a function of rate, temperature, and hydration. This data provided the foundation for the development of a constitutive model to describe the hygro-thermal elastic–viscoplastic stress–strain behavior of Nafion. The model was shown to capture the stress–strain behavior of Nafion over a wide range of uniaxial loadings histories. Here we assess the biaxial behavior of Nafion experimentally under different biaxiality ratios and then use the data to further validate the aforementioned constitutive model. Previous biaxial testing on Nafion has been reported for pressure loaded blister cells [3,4] which create an equibiaxial tensile stress at the center of the specimen, aimed at determining the stress at which gas leaks occur across the membrane. Biaxial testing has been conducted on a variety of other polymers such as poly(ethylene terephthalate) [5–8], polypropylene [9,10], polystyrene [11], polyethylene [12],

* Corresponding author.
*E-mail addresses:* meri.silberstein@gmail.com (M.N. Silberstein), mcboyce@mit.edu (M.C. Boyce).

0032-3861/$ – see front matter © 2010 Elsevier Ltd. All rights reserved.
doi:10.1016/j.polymer.2010.11.032

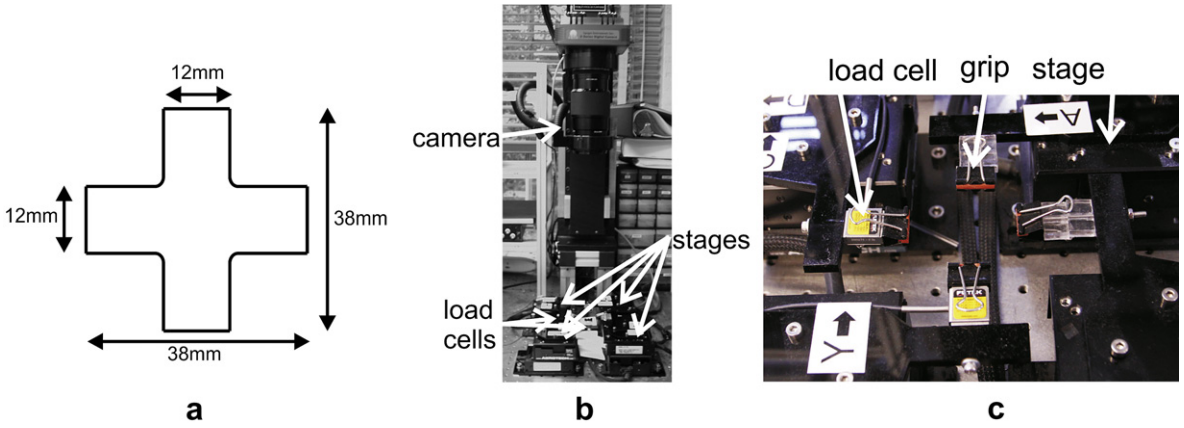


**Fig. 1.** Experimental setup for biaxial tensile tests (a) specimen shape (b) thin film multi-axial tensile machine (c) close up of stages from thin film multi-axial tensile machine.

and polyamide [12] for which biaxial draw is an important part of the manufacturing process. Most of these biaxial characterizations were conducted via in-plane extension devices which consist of many grips along each edge of a square specimen that can move independently in the two principal directions. With appropriate slitting or specimen design this can provide a close to homogeneous deformation with control over the degree of imposed biaxiality. In characterizing the biaxial behavior of metals, it is typical to use cruciform specimens with a single grip on each edge (i.e. Refs. [13–15]). The thickness in the central region of the specimen is reduced to ensure that the deformation is localized and slits are introduced in the legs for stress relief. In this paper, the cruciform configuration is used with a single grip on each edge of a uniform thickness specimen. This in-plane biaxial method also allows the desired control of the degree of biaxiality. The thickness reduction and slitting is not practical for the thin Nafion membrane ($t = 27$ μm), consequently the homogeneity of the resulting stress field will be discussed in depth in the results section.

## 2. Experimental methods

### 2.1. Materials

Commercially available dispersion cast NRE211 films (thickness $t = 27$ μm, Dupont, Ion Power Inc) and NRE212 films (thickness $t = 54$ μm, Dupont, Ion Power Inc) were used for the experimental characterization of Nafion. NRE211 and NRE212 are identical in chemical composition and processing, differing only in thickness. The films were stored in a desiccator cabinet upon removal from the initial packaging to minimize variability in data from aging and humidity effects.

### 2.2. Uniaxial tension

Uniaxial tension tests were conducted on Nafion NRE212 under monotonic, cyclic, stress relaxation, and creep histories, at constant engineering strain rates from 0.001 $s^{-1}$ to 0.1 $s^{-1}$, at temperatures from 25 °C to 100 °C, and at various water contents. The uniaxial results are presented in terms of time, true strain, and true stress as applicable. For full information on the uniaxial testing procedure and data reduction see Silberstein and Boyce [2].

### 2.3. Biaxial tension

Biaxial tests were performed on Nafion NRE211 laser cut into the cruciform shape shown in Fig. 1a. This particular cruciform geometry is chosen as a compromise between achieving a uniform stress field at the center of the specimen and reaching a reasonably large strain within the range of motion of the experimental setup. Biaxial tests were conducted on the thin film multi-axial tensile machine developed in the Bio-instrumentation lab at MIT (Fig. 1b) modified from the design of A. Herrmann in his master's thesis [16]. The film was gripped by rubber padded spring loaded clips. Each grip is mounted to an Aerotech ATS125 leadscrew-actuated stage and all actuators are moved such that the membrane center remains in place. For all tests the grips are initially 29 mm apart. Two of the grips are mounted to FUTEK LSB200 force sensors. The force and stage location are recorded at 1 s intervals. The deformation is monitored by an Apogee Alta U10 camera. A frame is recorded roughly every 10 s as limited by the capabilities of the acquisition system. The stage motion and data acquisition is controlled by a custom LabView code. The image frames are post-processed using the Vic2D strain analysis software to find local displacement values. The force-displacement and processed videos are then converted to the engineering stress components $\overline{\sigma}_{11}$ and $\overline{\sigma}_{22}$ using the initial cross-sectional area of the edge of the central square region (12 mm × 27 μm) and engineering strain values $\overline{\epsilon}_{11}$ and $\overline{\epsilon}_{22}$ in the biaxial region based on the markers near the edge of the region.

Monotonic experiments consist of grip displacement at a constant rate until reaching a preset displacement value. Cyclic experiments consist of grip displacement at a constant rate until reaching a preset displacement value, followed by grip displacement at the same constant rate in the opposite direction until the grips

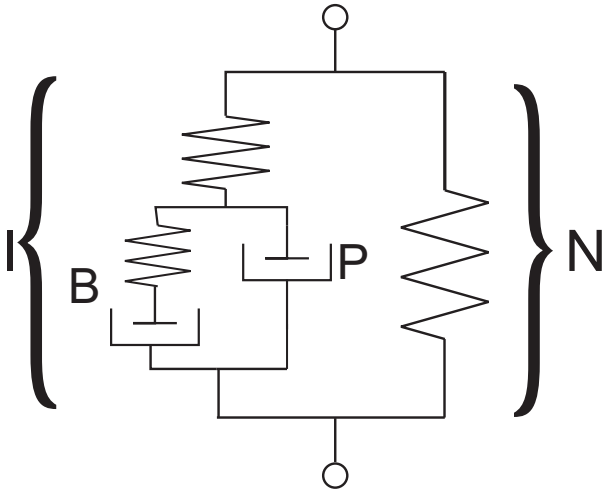


**Fig. 2.** Rheological depiction of Nafion constitutive model.

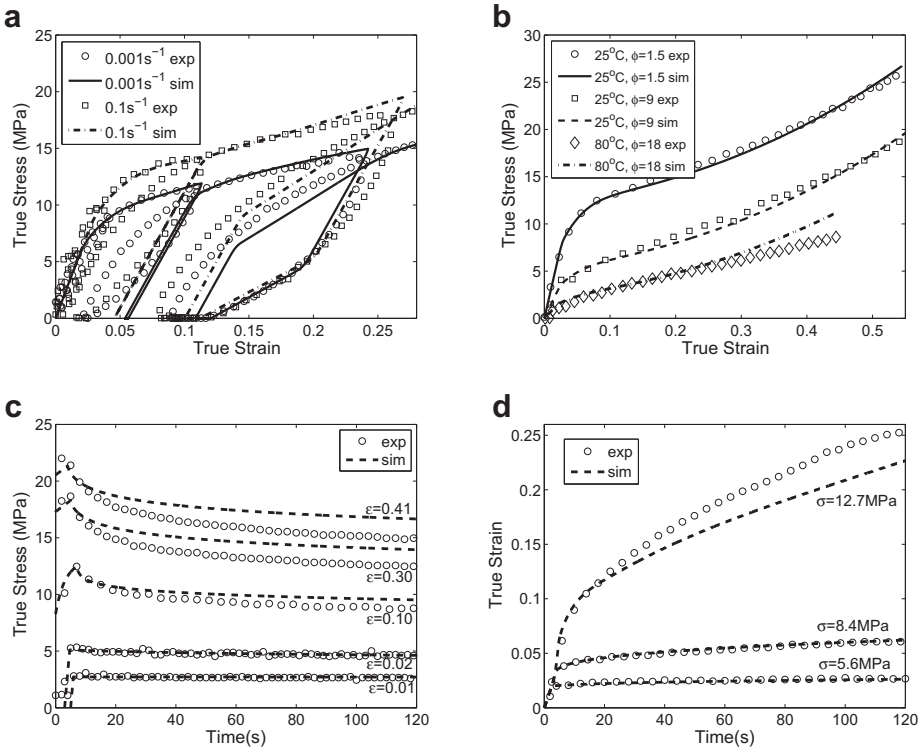


**Fig. 3.** Comparison of constitutive model predictions with experimental data for uniaxial tensile loading (a) cyclic rate dependence at ambient conditions ($\varphi = 1.5$) (b) temperature and hydration dependence at 0.01 $s^{-1}$ (c) stress relaxation at ambient conditions ($\varphi = 1.5$) (d) creep at ambient conditions ($\varphi = 1.5$).

return to their original location; this process is then repeated. It is typical for the specimens to buckle during the unloading process resulting in a near zero force. During this period the video extensometer continues to track the strain, however, due to the three dimensional nature of the deformation it does not indicate a local material strain.

## 3. Constitutive model review

In prior work of the authors a three dimensional constitutive model for Nafion was developed and implemented as a user material subroutine in the finite element program Abaqus [2]. Monotonic and cyclic uniaxial tension experiments over a range in strain rates and environmental conditions were used to fit and validate the model. This model and the experimentally observed uniaxial behavior will be briefly reviewed here to facilitate understanding of the results.

The elastic–viscoplastic constitutive model is depicted rheologically in Fig. 2, it consists of an intermolecular deformation mechanism (Mechanism I) acting in parallel with a molecular network alignment mechanism (Mechanism N). A summary of the model formulation is provided in the Appendix. The intermolecular

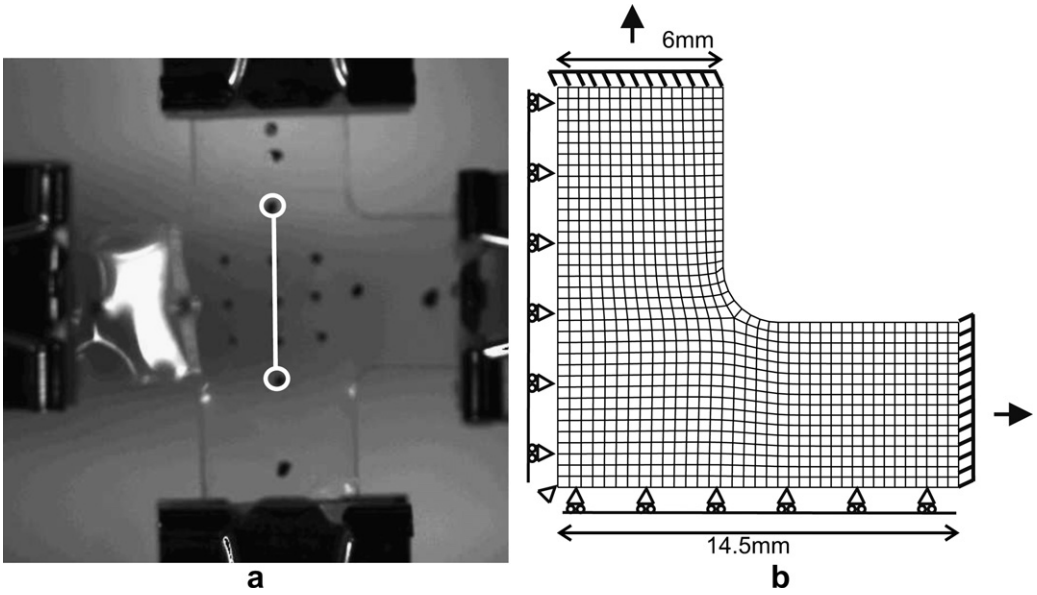


**Fig. 4.** (a) Specimen with line indicating location of points used for local strain measure of biaxial experiments. (b) Geometry and boundary constraints of biaxial simulation.

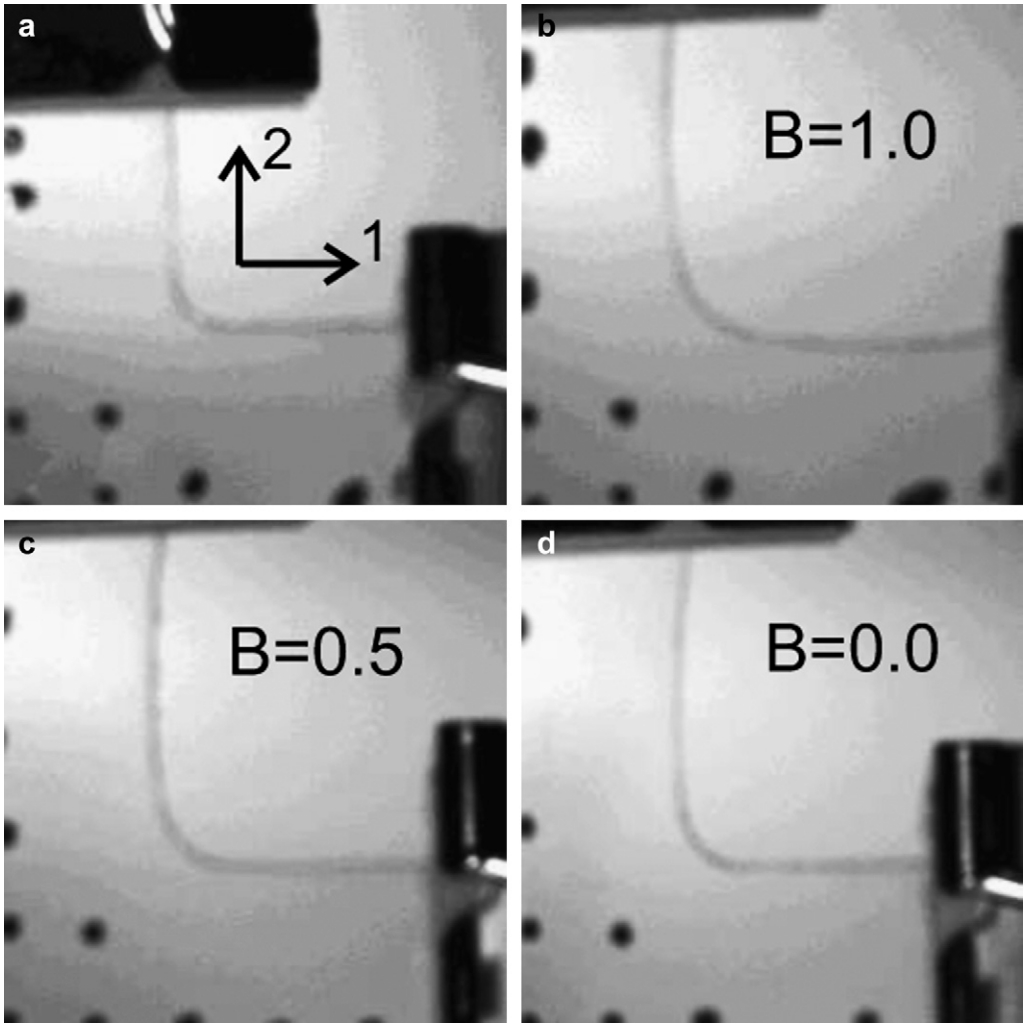


**Fig. 5.** Images of top right quarter of experimental biaxial specimens (a) typical specimen prior to deformation ($\bar{\epsilon}_{22} = 0$) (b) $B = 1.0$ specimen at 2-direction grip displacement = 2.5 mm ($\bar{\epsilon}_{22} = 0.05$) (c) $B = 0.5$ specimen at 2-direction grip displacement = 2.5 mm ($\bar{\epsilon}_{22} = 0.06$) (d) $B = 0.0$ specimen at 2-direction grip displacement = 2.5 mm ($\bar{\epsilon}_{22} = 0.08$).

mechanism, rheologically depicted as an elastic spring in series with a viscoplastic dashpot (P), represents the resistance to deformation due to the intermolecular interactions where the spring captures the stiffness of these interactions and the non-linear dashpot captures the yielding of these interactions. The intermolecular mechanism has a back stress (B) on the viscoplastic element which develops during loading to assist inelastic recovery. This back stress captures the inherent inhomogeneity of the local inelastic processes in polymers where a back stress builds around locally sheared domains; the existence of such stored energy which drives recovery has been experimentally found in calorimetry measurements (e.g. Refs. [17,18]) and modeled as a back stress in Ref. [19] and also more recently in Ref. [20]. The network mechanism is a non-linear spring which captures the resistance due to the stretching and orientation of the molecular network. The intermolecular resistance is strongly dependent on temperature and hydration, decreasing significantly when the polymer goes from the glassy state into the glass–rubber transition regime (~60 °C–120 °C). Hydration in the model is quantified as moles of water per mole of sulfonic acid group as is the custom in the Nafion literature (i.e. Ref. [21]). This quantity is given the symbol $\varphi$ and varies from ~1.5 at 25 °C, 30% relative humidity to ~22 at 90 °C and soaked in water. The model is presented in detail in Silberstein and Boyce [2].

A summary of results from this model compared with uniaxial tensile experimental data is shown in Fig. 3. The model is able to capture the linear-elastic response, the rate dependent distributed yield event, and the non-linear strain hardening under monotonic and cyclic tensile loading. Additionally it is able to capture the non-linear unloading and reloading observed to be characteristic of cyclic loading both as a function of strain and as a function of strain rate. The linear superposition of the effects of temperature and water content is seen to work well. The evolution of stress relaxation and creep through yield are also well predicted by the model.

## 4. Biaxial experiments: results and discussion

Cruciform specimens were subjected to three different biaxial loading conditions where the biaxiality ratio is described as the ratio of the stretching rates in the 1- and 2-directions ($B = \dot{\lambda}_1/\dot{\lambda}_2$). $B = 1.0$ corresponds to grips in both directions displaced at the same rate (14 μm $s^{-1}$), $B = 0.5$ corresponds to the 1-direction grips displaced at one-half the rate (7 μm $s^{-1}$) as the 2-direction grips (14 μm $s^{-1}$), and $B = 0.0$ corresponds to the 1-direction grips held fixed while the 2-direction grips are displaced (14 μm $s^{-1}$). The biaxial stress–strain response is determined from the strain in the central biaxial region calculated using the video extensometer points in the central square region of the specimen as indicated in

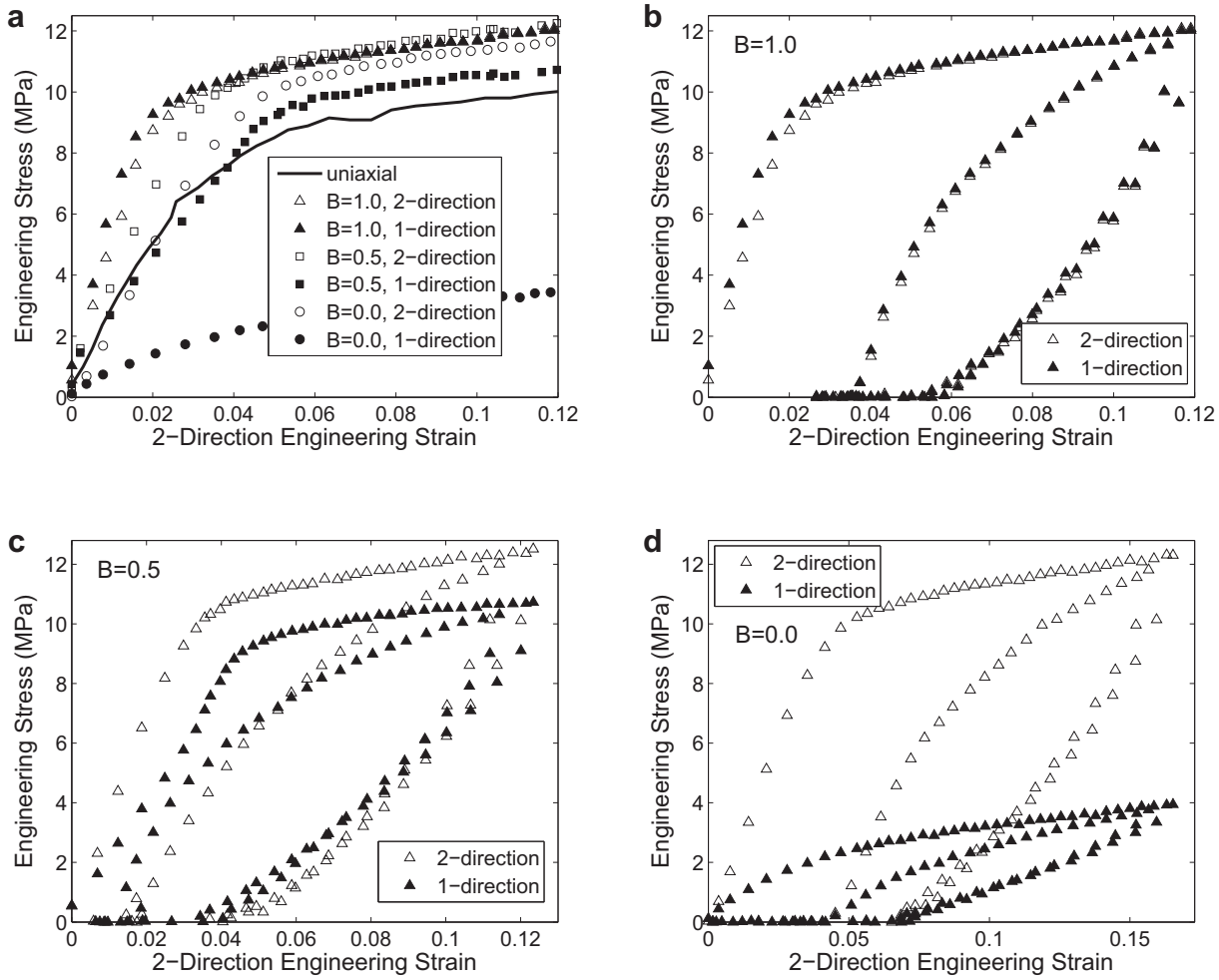


**Fig. 6.** Biaxial experimental data ($\varphi = 2$) (a) comparison of different degrees of biaxiality under monotonic loading (uniaxial data at $\varphi = 1.5$) (b) cyclic loading with 1- and 2-direction grips displaced at 14 μm $s^{-1}$ ($B = 1.0$) (c) cyclic loading with 2-direction grips displaced at 14 μm $s^{-1}$ and 1-direction grips displaced at 7 μm $s^{-1}$ ($B = 0.5$) (d) cyclic loading with 2-direction grips displaced at 14 μm $s^{-1}$ and 1-direction grips held fixed ($B = 0.0$).

Fig. 4a. The stress–strain behavior will be reported in terms of engineering stress versus engineering strain.

Images of the deformed specimen for all three cases are shown in Fig. 5; only the top right quarter is displayed in order to better correlate with the simulation images which will be shown subsequently. The character of the deformed shapes is most prominent in the legs of the cruciform since that is where the strain is largest. There is a distinct concave curvature between the grip and the central region in the 2-direction leg for all three cases and in the 1-direction leg for $B = 1.0$; this curvature is clearly absent in the 1-direction leg for $B = 0.0$.

Fig. 6a shows the monotonic biaxial engineering stress–strain response of all three cases compared to the uniaxial tensile behavior. In all cases the stress–strain behavior exhibits an elastic–plastic response with features similar to the uniaxial behavior. The biaxial effect on the stress–strain response is apparent. For the case of equibiaxial ($B = 1.0$) loading, the initial elastic stiffness is greater than the uniaxial stiffness, as expected (recall, the biaxial modulus is $E/(1-\nu)$ compared to the uniaxial modulus $E$). The yield stress level required for biaxial yielding is also greater than for uniaxial yielding which is unexpected; the biaxial stress components at yield for equibiaxial tension would be expected to be equal to the uniaxial yield following a Mises or Tresca yield criterion (they would be expected to be lower if there were a pressure dependence). The unexpected disparity in yield stress between the uniaxial and equibiaxial experiments is a result of: (1) the inhomogeneous stress distribution in the central region of the cruciform which produces a sharper yield transition in the reduced data; and (2) the rollover nature of the yield event which occurs more rapidly with biaxial loading as compared to uniaxial loading. Thus even though yield is technically initiating at the same value for equibiaxial as for uniaxial loading, this very initial yielding cannot be observed directly by this experiment. The specimen geometry effect will be discussed further in Section 5. There is also a minor strain rate effect since the effective rate driving yield is larger for the equibiaxial case than the uniaxial case, but this is negligible in comparison to the effects of either geometry or rollover yield evolution.

The $B = 0.5$ and the $B = 0.0$ results also reveal the effect of biaxiality on initial stiffness, the yield, and post-yield behavior as well as the dramatically different $\sigma_{11}$ and $\sigma_{22}$ histories for these non-equibiaxial conditions. In the 2-direction the $B = 0.5$ and the $B = 0.0$ responses follow the trend of the $B = 1.0$ and uniaxial ($B \sim -0.5$) responses with the initial stiffness, yield stress, and post-yield hardening decreasing monotonically from $B = 1.0$ to $B = -0.5$. The stress response in the 1-direction decreases as expected going from $B = 1.0$ to $B = 0.5$ to $B = 0.0$ since there is less strain applied in that direction. The cyclic behavior is shown in Fig. 6b–d for the $B = 1.0$, $B = 0.5$, and $B = 0.0$ cases, respectively. In each case for both the 1- and 2-directions there is a non-linear unloading and reloading with a reduced yield upon reloading,

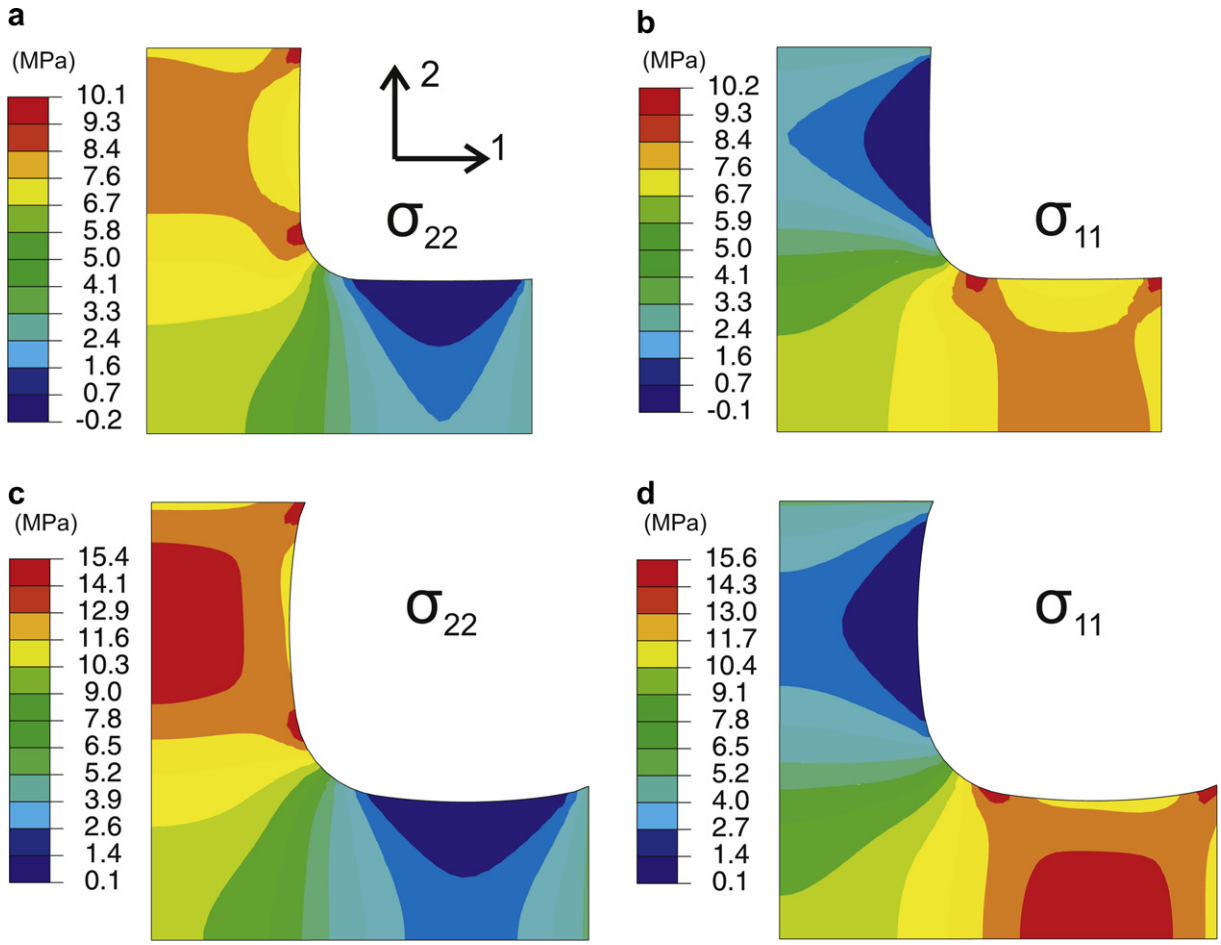


**Fig. 7.** Stress contours from simulated equibiaxial tensile loading ($B = 1.0$) for the 1- and 2-direction grips extended at 14 μm $s^{-1}$: prior to yield (2-direction grip displacement = 0.42 mm) (a) $\sigma_{22}$ ($\bar{\sigma}_{22} = 8.0$) (b) $\sigma_{11}$ ($\bar{\sigma}_{11} = 8.0$) and just after yield (2-direction grip displacement = 2.5 mm) (c) $\sigma_{22}$ ($\bar{\sigma}_{22} = 10.7$) (d) $\sigma_{11}$ ($\bar{\sigma}_{11} = 10.7$).

much as observed earlier in uniaxial tension. The specimens buckle during the process of returning the grips to their initial locations. Further strain recovery is seen to occur in the buckled state, resulting in reloading initiating from a lower strain than that at which zero strain was reached during unloading.

## 5. Biaxial modeling: results and discussion

Finite element simulations of each of the biaxial loading tests are conducted. The symmetry of the tests enables a one-fourth model of the specimen with appropriate boundary conditions as shown in Fig. 4b; a mesh convergence study was conducted to assess the quality of the mesh. The material behavior is modeled using the constitutive model with the properties determined from uniaxial tests obtained in Silberstein and Boyce [2]. Contours of $(\sigma_{11})$ and $(\sigma_{22})$ in the elastic regime and just past yield are shown for the $B = 1.0$, $B = 0.5$, and $B = 0.0$ cases in Figs. 7–9, respectively. First, we note that the deformed shape just past yield for each of these figures matches well with the corresponding experimental images taken at the same grip displacement. As in the experiments, there is a distinct concave curvature between the grip and the central region in the 2-direction leg for all three cases and the 1-direction leg for $B = 1.0$ and this curvature is clearly absent in the 1-direction for $B = 0.0$. Second, even though the cruciform specimen shape was chosen to achieve a uniform biaxial stress state at the central region, it is clear from these simulations that this is not the case. The stress varies by approximately 25% across this central region. It is therefore critical that the finite element results are reduced to biaxial stress–strain results in the same manner as the experimental results for any direct comparison: the reaction forces are measured at the grips and strains are measured from the displacement of points just outside the central square biaxial region. The model results are found to well predict the loading portion of the experimental results in all three cases (Fig. 10). The simulations capture the initial stiffness, the yield, and the post-yield behavior as observed for $(\bar{\sigma}_{11})$ and $(\bar{\sigma}_{22})$ histories for all three biaxial conditions, indicating high accuracy of the model in predicting biaxial loading. The unloading and reloading slopes in the model appear to be stiffer than in the experiments. Interestingly, the unload and reload yield shoulders occur as the same stress as in the experiments. This model therefore seems to underestimate the gradual nature of both the forward and reverse plastic deformation processes. The model also underpredicts the strain recovery of the specimen in the buckled state prior to reloading. The magnitude of the uncaptured strain recovery is similar in all cases ($\bar{\epsilon} \sim 0.015$). While the origin of this disparity is not known at this time, it does not appear to be specific to multi-axial loading. We can see that the framework used to incorporate the uniaxial behavior into a three dimensional model is in fact capable of predicting the multi-axial deformation response of the membrane.

As discussed above, this particular geometry does not provide a perfect homogeneous biaxial stress distribution within the central region. In order to understand the biaxial test itself better and the accuracy of the data for providing the material

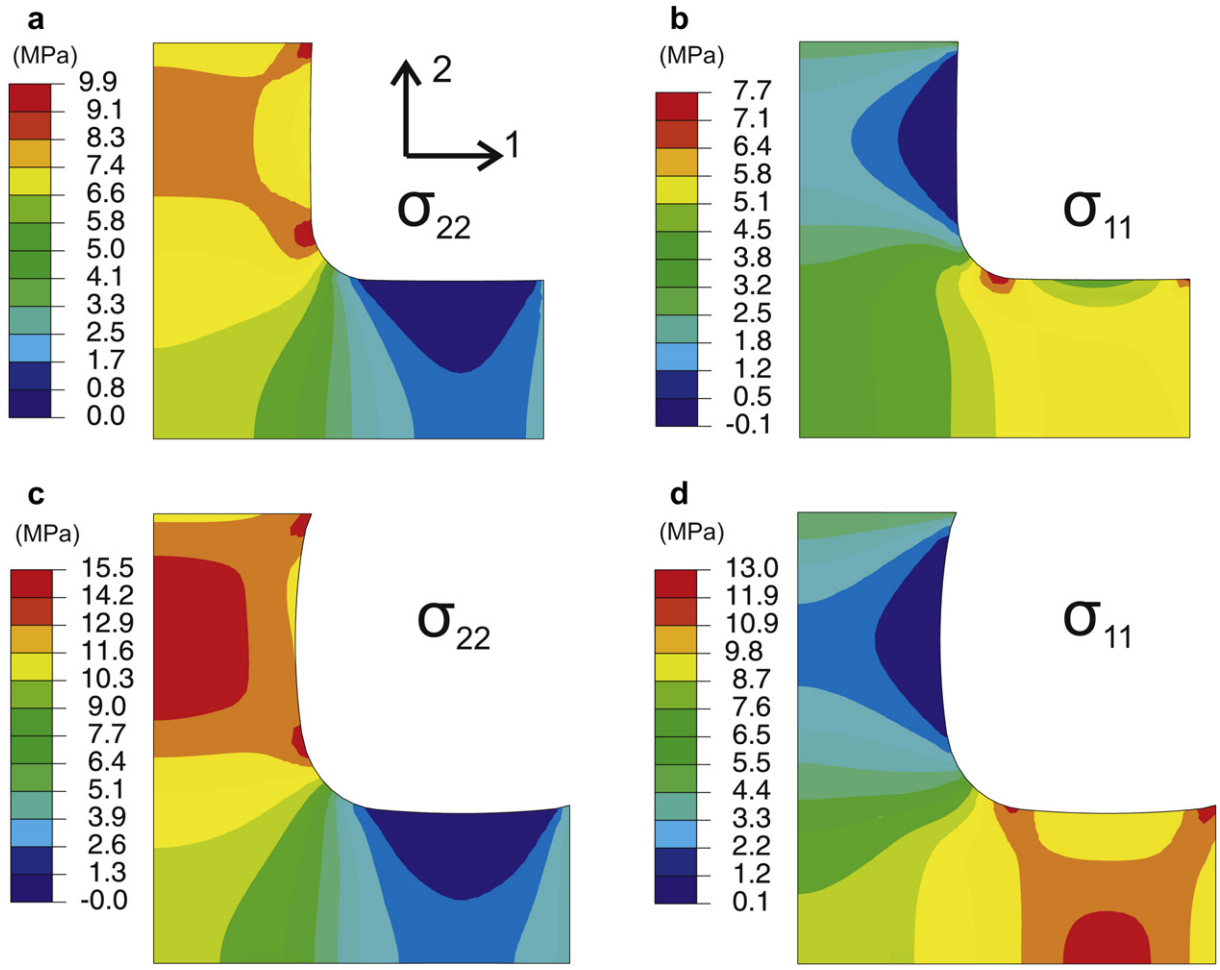


**Fig. 8.** Stress contours from simulated biaxial tensile loading ($B = 0.5$) for the 2-direction grips extended at 14 μm $s^{-1}$ and 1-direction grips extended at 7 μm $s^{-1}$: prior to yield (2-direction grip displacement = 0.42 mm) (a) $\sigma_{22}$ ($\bar{\sigma}_{22} = 7.8$) (b) $\sigma_{11}$ ($\bar{\sigma}_{11} = 5.4$) and just after yield (2-direction grip displacement = 2.5 mm) (c) $\sigma_{22}$ ($\bar{\sigma}_{22} = 10.7$) (d) $\sigma_{11}$ ($\bar{\sigma}_{11} = 9.6$).

stress–strain response under different biaxial histories, we compare the stress–strain histories reduced from the test simulation with the model predictions of the corresponding pure homogeneous strain histories (Fig. 11). The homogeneous simulations are run with the 2-direction strain rate matched to the initial $\bar{\epsilon}_{22}$ rate of the cruciform. The strain rate variation in $\bar{\epsilon}_{22}$ which never exceeds a factor of three was neglected. Looking first at $\sigma_{22}$ (Fig. 11a), it is evident that the cruciform specimen provides an accurate measure of the elastic regime. However, the yield event occurs in a sharper manner and at a higher stress as compared to the homogeneous response indicating that reduction of the cruciform data loses some of the details of the distributed yield event. The cruciform specimen also results in an exaggerated difference in the stress response of $B = 1.0$, $B = 0.5$, and $B = 0.0$ around the yield event. An increase in the magnitude and sharpness of yield is also evident in each of the ($\sigma_{11}$) responses (Fig. 11b–d). For completeness we also include the simulated uniaxial response at a strain rate matching the 2-direction rate of the homogeneous biaxial simulations. Comparing the homogeneous equibiaxial stress–strain response to the uniaxial stress–strain response, it is evident that yield initiates at roughly the same stress for these two loading histories, but the hardening evolves more rapidly for the equibiaxial case, initially as a result of the greater effective strain rate (and hence the greater effective strain at any given axial strain where the yield stress evolves with effective strain) and then as a result of the network stretch. These simulation results indicate that while the experimental data is generally capturing the biaxial material response, it would not be appropriate for direct evaluation of the biaxial yield stress or post-yield tangent modulus. Conversely, this method is quite appropriate for model validation since it requires the model to capture not only the homogeneous biaxial response but also the effects of stress and strain distributions.

## 6. Conclusions

The behavior of Nafion was experimentally explored under tensile biaxial loading conditions varying the degree of biaxiality. Biaxial testing was conducted via in-plane tensile testing of cruciform shaped specimens. A video extensometer system was used to enable determination of the local biaxial response in the central region. The biaxial response was qualitatively similar to the uniaxial response with the stiffness and strength in a given direction dependent on the degree of biaxiality. A three dimensional hygro-thermal elastic–viscoplastic constitutive model developed for Nafion based on uniaxial tensile data was used to simulate these experiments via a finite element implementation. These simulations revealed that the stress distribution is not completely uniform in the central "biaxial" region of the specimen. The cruciform specimens result in a greater and sharper yield event as compared to the pure homogeneous biaxial response. Nonetheless, the constitutive model was shown to well predict this complex multi-axial deformation response when the model is implemented in the

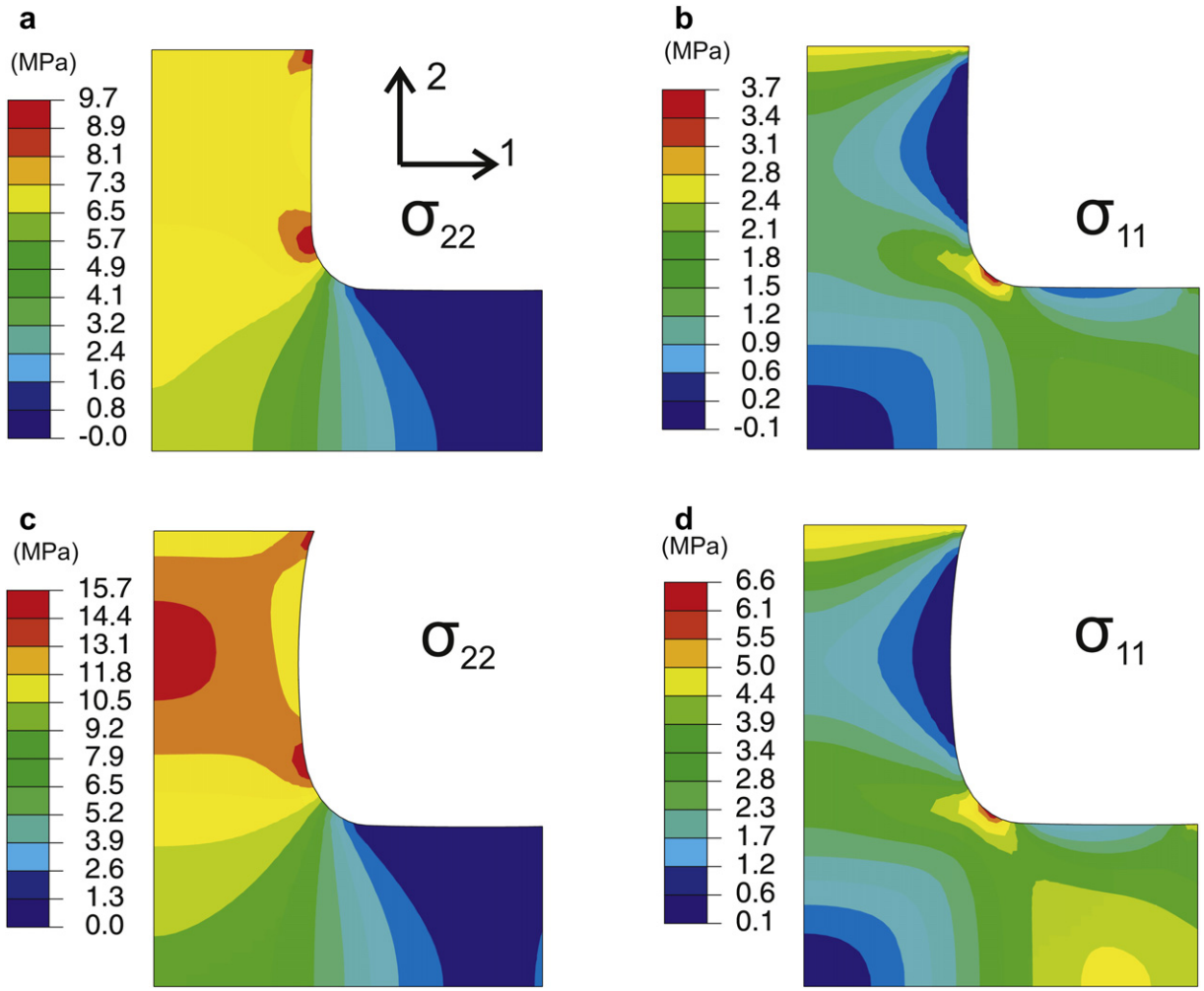


**Fig. 9.** Stress contours from simulated biaxial tensile loading ($B = 0.0$) for the 2-direction grips extended at 14 μm $s^{-1}$ and 1-direction grips held fixed: prior to yield (2-direction grip displacement = 0.42 mm) (a) $\sigma_{22}$ ($\bar{\sigma}_{22} = 7.3$) (b) $\sigma_{11}$ ($\bar{\sigma}_{11} = 1.6$) and just after yield (2-direction grip displacement = 2.5 mm) (c) $\sigma_{22}$ ($\bar{\sigma}_{22} = 10.6$) (d) $\sigma_{11}$ ($\bar{\sigma}_{11} = 3.6$).

experimental geometry and reduced by the same methods as the experimental results. These results also indicated that while the initial yield under equibiaxial and uniaxial loading conditions are the same, the evolution in strength with strain (the rollover nature of yield) gives the appearance of a greater yield stress during biaxial loading compared to uniaxial loading – an effect captured by the model. It should be noted that no material parameters were modified to fit the biaxial data, the success therefore demonstrates the truly predictive capability of the model. The biaxial testing method and predictive constitutive modeling have broad relevance to polymeric membranes, especially considering the need for robustness to biaxial loading for polymer membranes in a wide range of separation and transport processes.

## Acknowledgements

Funding for this work was provided by the Institute for Soldier Nanotechnologies, NSF grant CMMI-0700414, and the Masdar Institute.

## Appendix. Constitutive model at constant temperature and hydration

A rheological schematic of the elastic–viscoplastic constitutive model for Nafion is shown in Fig. 2 in the main body of the text. A fundamental assumption in the model structure is that the stress response of a material can be decomposed into multiple mechanisms. In this case two mechanisms are needed to model the material behavior: Mechanism I, rheologically depicted as an elastic spring in series with a viscoplastic dashpot, represents the resistance to deformation due to the intermolecular interactions where the spring captures the stiffness of these interactions and the non-linear dashpot captures the yielding of these interactions; Mechanism N is a non-linear spring which represents a resistance due to the stretching and orientation of the molecular network.

The model is fully three dimensional but will be expressed in principal stretch space for simplicity. Throughout this discussion $i = 1,2,3$ are taken to indicate the three principal stretch directions with no sum on repeated $i$ unless otherwise noted. The macroscopic deformation is given by the principal stretches $\lambda_i$. Each mechanism is taken to experience the same deformation and the total stress acting on the system is equal to the sum of the contributions from each mechanism:

$$\lambda_{Ii} = \lambda_{Ni} = \lambda_i \tag{1}$$

$$T_i = T_{Ii} + T_{Ni} \tag{2}$$

where $\lambda_{Ii}$ and $\lambda_{Ni}$ are the principal stretches of the intermolecular ($I$) and network ($N$) mechanisms, respectively, and $T_{Ii}$ and $T_{Ni}$ are the Cauchy (true) stress contributions of the intermolecular and

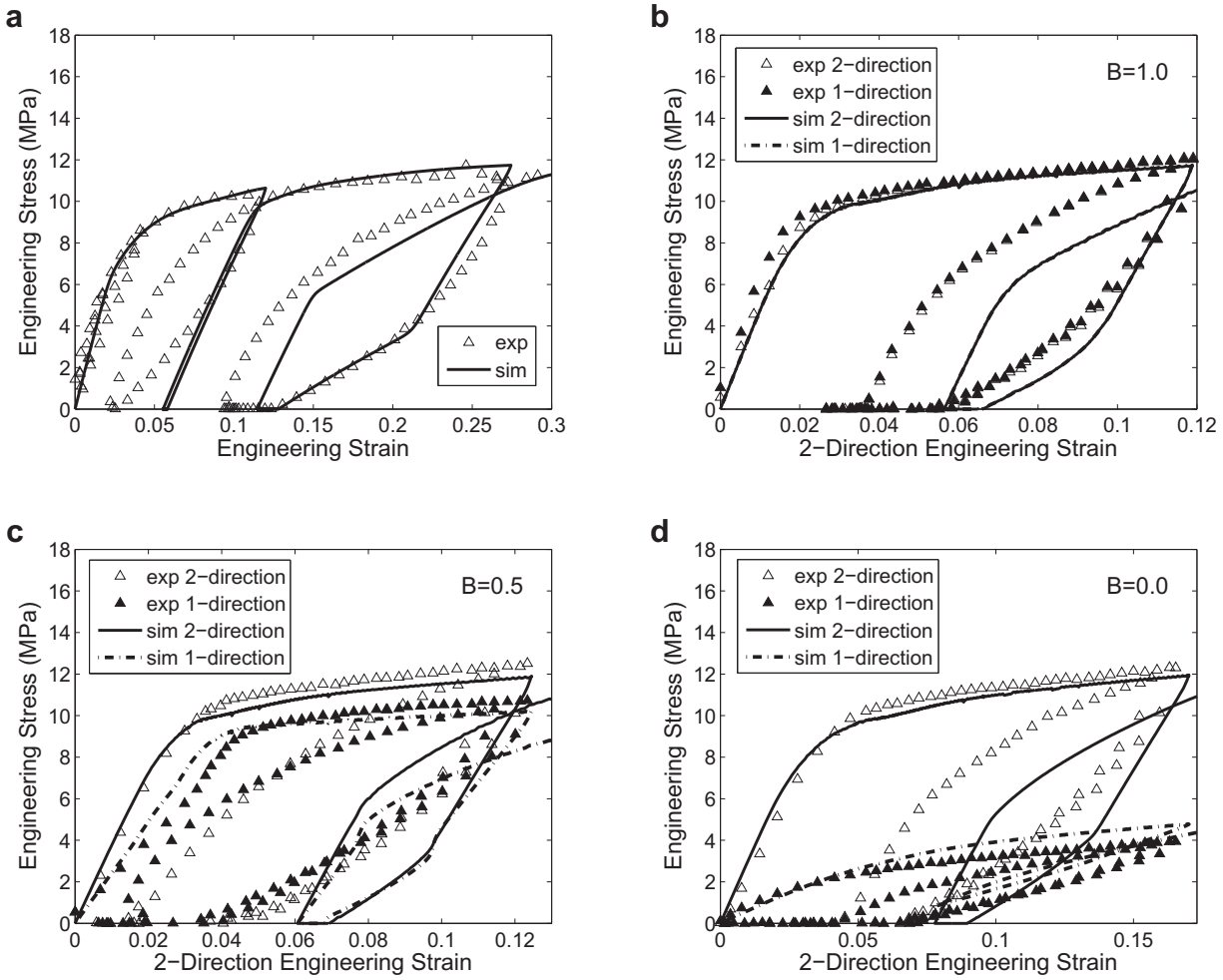


**Fig. 10.** Model compared to experimental data for biaxial tensile loading using video extensometer equivalent strain measure (a) uniaxial behavior for reference ($\phi = 1.5$) (b) 1- and 2-direction grips displaced at 14 μm s$^{-1}$ ($B = 1.0$, $\phi = 2$) (c) 2-direction grips displaced at 14 μm s$^{-1}$ and 1-direction grips displaced at 7 μm s$^{-1}$ ($B = 0.5$, $\phi = 2$) (d) 2-direction grips displaced at 14 μm s$^{-1}$ and 1-direction grips held fixed ($B = 0.0$, $\phi = 2$).

network mechanisms, respectively. The governing equations for each mechanism are given below followed by a table listing the values used for the material parameters (Table 1).

*Mechanism N*: The stress arising from the network resistance to deformation ($T_{Ni}$) is taken to be deviatoric and is derived from the resistance to stretching and orientation of the molecular network; here we use the Neo-Hookean model:

$$T_{Ni} = \frac{1}{J}\mu_N B'_{Ni} \tag{3}$$

where $J = \lambda_1\lambda_2\lambda_3$ is the volume ratio, $\mu_N$ is the rubbery shear modulus, and $B'_{Ni}$ is the deviatoric part of the Cauchy Green tensor given by $B'_{Ni} = \lambda^2_{Ni} - \lambda^2_{\text{chain}}$ . $\lambda_{\text{chain}} = \sqrt{\left(\lambda_1^2+\lambda_2^2+\lambda_3^2\right)/3}$ is a measure of network stretch.

*Mechanism I*: At ambient temperatures, the intermolecular mechanism provides an initially relatively stiff response followed by yielding and post-yield flow. To capture the elastic–plastic nature of the deformation, the stretch is decomposed into elastic and plastic components using the Kroner-Lee multiplicative decomposition $\lambda_{Ii} = \lambda^e_{Ii}\lambda^p_{Ii}$ where $\lambda^e_{Ii}$ are the elastic stretches and $\lambda^p_{Ii}$ are the plastic stretches. The plastic deformation is taken to be isochoric giving the plastic volume ratio $J^p = \lambda^p_1\lambda^p_2\lambda^p_3 = 1$. The intermolecular contribution to the Cauchy (true) stress is found from a generalized Hookean relationship:

$$T_{Ii} = \frac{1}{J^e}\left[2\mu\left(\ln\lambda^e_{Ii}\right)' + \kappa \ln J^e\right] \tag{4}$$

where $J^e = \lambda^e_{I1}\lambda^e_{I2}\lambda^e_{I3}$ is the elastic mechanical volume ratio, $\mu$ is the shear modulus, and $\kappa$ is the bulk modulus.

*Plastic Flow*: To obtain the decomposition of $\lambda_{Ii}$ into $\lambda^e_{Ii}$ and $\lambda^p_{Ii}$, the rate kinematics are needed where the velocity gradient is given by

$$D_{Ii} = \dot{\lambda}_{Ii}\lambda^{-1}_{Ii} \tag{5}$$

$D_{Ii}$ is further decomposed into elastic and plastic quantities

$$D_{Ii} = D^e_{Ii} + D^p_{Ii} \tag{6}$$

where $D^e_{Ii}$ is the elastic velocity gradient and $D^p_{Ii}$ is the plastic velocity gradient. $D^p_{Ii}$ is constitutively prescribed below. Initially, plastic flow is driven by the deviator of the stress $T_{Ii}$. Once plastic flow ensues, a back stress $T_{Bi}$ develops around locally deforming sites; this back stress drives reverse plasticity and the corresponding highly non-linear unloading. Therefore, the driving stress for plastic flow is the deviator of the stress difference $(T_{Ii} - T_{Bi})$. Hence, $D^p_{Ii}$ is constitutively defined to follow a thermally activated flow process driven by $T_{Ii} - T_{Bi}$.

$$D^p_{Ii} = \dot{\gamma}^p_I \frac{T'_{Pi}}{\sqrt{2}\tau_P} \tag{7}$$

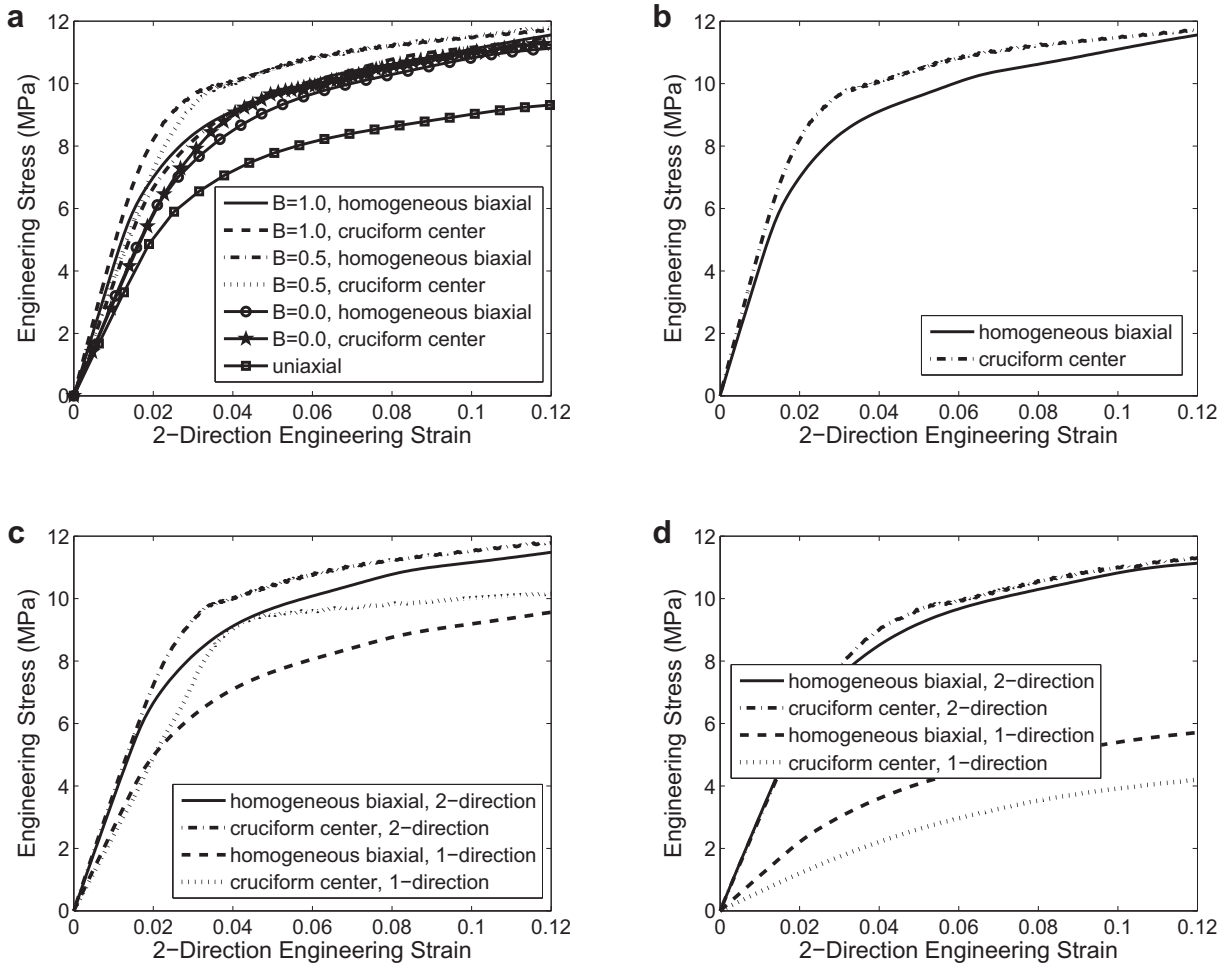


**Fig. 11.** Comparison of simulation result for pure homogeneous biaxial deformation with simulation result for biaxial deformation as conducted experimentally with the cruciform specimen ($\phi = 2$) (a) $\bar{\sigma}_{22}$ for all three degrees of biaxiality (b) 1- and 2-direction grips displaced at 14 μm s$^{-1}$ ($B = 1.0$) (c) 2-direction grips displaced at 14 μm s$^{-1}$ and 1-direction grips displaced at 7 μm s$^{-1}$ ($B = 0.5$) (d) 2-direction grips displaced at 14 μm s$^{-1}$ and 1-direction grips held fixed ($B = 0.0$).

$$\dot{\gamma}_I^p = \dot{\gamma}^o \exp\left[\frac{-\Delta G}{k_b\theta}\right] \sin h\left[\frac{\Delta G}{k_b\theta}\frac{\tau_P}{s}\right] \tag{8}$$

$$T'_{Pi} = (T_{Ii} - T_{Bi})' \tag{9}$$

$$T'_{Bi} = \frac{1}{J} 2\mu_B \ln\lambda^e_{Bi} \tag{10}$$

**Table 1**
Material parameters for Nafion constitutive model.

| Model component | Material parameter | Value |
|---|---|---|
| Elastic | $\kappa$ | $3.3 \times 10^8$ Pa |
| | $\mu_o$ | $1.1 \times 10^8$ Pa |
| Elastic evolution | $h$ | $4.7 \times 10^9$ Pa |
| | $\mu_{sat}$ | $7.0 \times 10^7$ Pa |
| Rate dependent yield | $\dot{\gamma}^o$ | 6.72 s$^{-1}$ |
| | $\Delta G$ | $8.98 \times 10^{-20}$ J |
| | $\tilde{s}_o$ | $6.5 \times 10^6$ Pa |
| Distributed yield | $\tilde{h}$ | $1.2 \times 10^9$ Pa |
| | $\tilde{s}_{sat}$ | $9.6 \times 10^6$ Pa |
| | $\hat{h}$ | $7.5 \times 10^7$ Pa |
| | $\hat{s}_{sat}$ | $6.5 \times 10^6$ Pa |
| Isotropic hardening | $\bar{h}$ | $2.6 \times 10^7$ Pa |
| | $\bar{n}$ | 1 |
| Back stress | $\mu_B$ | $2.65 \times 10^7$ Pa |
| | $s_{Bo}$ | $4.3 \times 10^6$ Pa |
| | $h_B$ | $2.3 \times 10^8$ Pa |
| | $s_{Bsat}$ | $7.7 \times 10^6$ Pa |
| Network | $\mu_N$ | $3.3 \times 10^6$ Pa |

where $\dot{\gamma}_I^p$ is the magnitude of the plastic velocity gradient, $\tau_P = \sqrt{1/2(T'^2_{P1} + T'^2_{P2} + T'^2_{P3})}$ is the scalar equivalent shear stress, $\dot{\gamma}^o$ is a pre-exponential factor proportional to the attempt frequency, $\Delta G$ is the activation energy, $s$ is the isotropic shear resistance, $k_b$ is Boltzmann's constant, $\theta$ is the absolute temperature, $\mu_B$ is the back stress shear modulus, and $\lambda^e_{Bi}$ is the elastic portion of the back stress stretch to be discussed shortly.

The plastic stretch is found by integrating $\dot{\lambda}^p_{Ii} = D^p_{Ii}\lambda^p_{Ii}$. The elastic stretch is then calculated by $\lambda^e_{Ii} = \lambda_{Ii}(\lambda^p_{Ii})^{-1}$.

*Distributed yield event*: The yield process is observed to be a distributed event as evident by the gradual rollover nature of yielding. This distributed aspect of yield could be captured by numerous dashpots of different energy barriers in parallel; however, for simplicity, this is captured by an evolution in strength $s$ with plastic flow. $s$ evolves throughout the deformation process, with an initial increase during yield ($\tilde{s}$), a softening with further plasticity ($\hat{s}$), and an increase with network alignment ($\bar{s}$). The initial shear resistance $\tilde{s}_o$ is taken to increase with $\dot{\gamma}^p_I$ until reaching a saturated state during plastic deformation reflecting the distributed nature of yield.

$$\dot{\tilde{s}} = \tilde{h}\left(1 - \frac{\tilde{s}}{\tilde{s}_{sat}}\right)\dot{\gamma}^p_I \tag{11}$$

where $\tilde{h}$ controls the rate of approach of $\tilde{s}$ to its saturation value $\widehat{s}_{sat}$. To capture a softening that occurs upon percolation, $s_o = 0$, which is subtracted from $\tilde{s}$, is taken to increase with $\dot{\gamma}_I^p$ at a slower rate than $\tilde{s}$, to its saturated value $\widehat{s}_{sat}$.

$$\dot{\widehat{s}} = h\left(1 - \frac{\widehat{s}}{\widehat{s}_{sat}}\right)\dot{\gamma}_I^p \tag{12}$$

where $h$ controls the rate of approach of $\widehat{s}$ from its initial value of 0 to its saturation value $\widehat{s}_{sat}$.

*Post-yield isotropic hardening*: Molecular alignment provides an additional increase to the intermolecular shear resistance captured by the contribution $\bar{s}$.

$$\bar{s} = \bar{h}\left(\lambda_{\text{chain}}^{\bar{n}} - 1\right) \tag{13}$$

where $\bar{h}$ controls the initial slope and $\bar{n}$ controls the nonlinearity. The strength ($s$) is then given by:

$$s = \tilde{s} - \widehat{s} + \bar{s}. \tag{14}$$

*Saturation of the intermolecular back stress*: The back stress is observed to saturate as evident by the nonlinearity of the unloading curves and as also found in calorimetry measurements on other polymers [17]. This is captured by the dashpot on the back stress element. The back stretch $\lambda_{Bi}$ is therefore separated into elastic and plastic components using the Kroner-Lee multiplicative decomposition $\lambda_{Bi} = \lambda_{Bi}^e \lambda_{Bi}^p$ where $\lambda_{Bi}^e$ are the elastic stretches and $\lambda_{Bi}^p$ are the plastic stretches. The rate kinematics are needed where the velocity gradient is given by

$$D_{Bi} = \dot{\lambda}_{Bi}\lambda_{Bi}^{-1} \tag{15}$$

$D_{Bi}$ is further decomposed into elastic and plastic quantities

$$D_{Bi} = D_{Bi}^e + D_{Bi}^p \tag{16}$$

where $D_{Bi}^e$ is the elastic velocity gradient and $D_{Bi}^p$ is the plastic velocity gradient. The back stress saturation dashpot is prescribed to evolve according to:

$$D_{Bi}^p = \dot{\gamma}_B^p \frac{T'_{Bi}}{\sqrt{2}\tau_B} \tag{17}$$

$$\dot{\gamma}_B^p = \dot{\gamma}^o \exp\left[-\frac{\Delta G}{k_b\theta}\right] \sin h\left[\frac{\Delta G}{k_b\theta}\frac{\tau_B}{s_B}\right] \tag{18}$$

where $\tau_B = \sqrt{1/2(T'^2_{B1} + T'^2_{B2} + T'^2_{B3})}$ is the corresponding equivalent shear stress and $s_B$ is the isotropic back stress saturation strength. $\dot{\gamma}^o$ and $\Delta G$ are the same constants as for the intermolecular plastic deformation since the rate dependence of unloading is similar to that of loading. $s_B$ is taken to evolve to a maximum with $\dot{\gamma}_B^p$ such that the saturation of the back stress occurs gradually.

$$\dot{s}_B = h_B\left(1 - \frac{s_B}{s_{Bsat}}\right)\dot{\gamma}_B^p \tag{19}$$

where $h_B$ controls the evolution with shear and $s_{Bsat}$ is the saturation value.

The plastic back stretch is found by integrating $\dot{\lambda}_{Bi}^p = D_{Bi}^p \lambda_{Bi}^p$. The elastic back stretch is then calculated by $\lambda_{Bi}^e = \lambda_{Bi}(\lambda_{Bi}^p)^{-1}$.

## References


[1] Borup R, Meyers J, Pivovar B, Kim YS, Mukundan R, Garland N, et al. Chemical Reviews 2007;107:3904–51.
[2] Silberstein MN, Boyce MC. Journal of Power Sources 2010;195:5692–706.
[3] Dillard DA, Li YQ, Grohs JR, Case SW, Ellis MW, Lai YH, et al. Journal of Fuel Cell Science and Technology 2009;6:031014-1–031014-8.
[4] Li YQ, Dillard DA, Case SW, Ellis MW, Lai YH, Gittleman CS, et al. Journal of Power Sources 2009;194:873–9.
[5] Matthews RG, Duckett RA, Ward IM, Jones DP. Polymer 1997;38:4795–802.
[6] Adams AM, Buckley CP, Jones DP. Polymer 1998;39:5761–3.
[7] Gerlach C, Buckley CP, Jones DP. Chemical Engineering Research and Design 1998;76:38–44.
[8] Adams AM, Buckley CP, Jones DP. Polymer 2000;41:771–86.
[9] Sweeney J, Collins TLD, Coates PD, Ward IM. Polymer 1997;38:5991–9.
[10] Sweeney J, Spares R, Woodhead M. Polymer Engineering and Science 2009;49:1902–8.
[11] Zhang XM, Ajji A. Journal of Applied Polymer Science 2003;89:487–96.
[12] Zeng FF, Le Grognec P, Lacrampe MF, Krawczak P. Mechanics of Materials 2010;42:686–97.
[13] Makinde A, Thibodeau L, Neale KW. Experimental Mechanics 1992;32:138–44.
[14] Demmerle S, Boehler JP. Journal of Mechanics and Physics of Solids 1993;41:143–81.
[15] Hannon A, Tiernan P. Journal of Materials Processing Technology 2008;198:1–13.
[16] Herrmann AM, MS thesis, Cambridge, MA: Massachusetts Institute of Technology; February 2006.
[17] Hasan OA, Boyce MC. Polymer 1993;34:5085–92.
[18] Salamantina OB, Rudnev SN, Voenniy VV, Oleynik EF. Journal of Thermal Analysis 1992;38:1271–81.
[19] Hasan OA, Boyce MC. Polymer and Engineering Science 1995;35:331–44.
[20] Anand L, Ames NM, Srivastava V, Chester SA. International Journal of Plasticity 2009;25:1474–94.
[21] Kusoglu A, Karlsson AM, Santare MH. Polymer 2010;51:1457–64.